



Convoluting models and high-Weissenberg predictions for micellar thixotropic fluids in contraction–expansion flows



J.E. López-Aguilar^a, M.F. Webster^{a,*}, H.R. Tamaddon-Jahromi^a, O. Manero^b

^aInstitute of Non-Newtonian Fluid Mechanics, College of Engineering, Swansea University, Bay Campus, Fabian Way, Swansea SA1 8EN, United Kingdom

^bInstituto de Investigaciones en Materiales, UNAM, 04510, Mexico

ARTICLE INFO

Article history:

Received 14 July 2015

Revised 4 March 2016

Accepted 6 March 2016

Available online 12 March 2016

Keywords:

High-elasticity solutions

Wormlike micelles

Convoluting EPTT-Bautista–Manero models

Numerical simulation

Hybrid finite element/volume method

Enhanced oil-recovery

ABSTRACT

This study is concerned with finite element/volume modelling of contraction–expansion axisymmetric pipe flows for thixotropic and non-thixotropic viscoelastic models. To obtain solutions at high Weissenberg numbers (Wi) under a general differential form $Wi \overset{\nabla}{\tau}_p = 2(1 - \beta)\mathbf{D} - f\tau_p$, both thixotropic Bautista–Manero micellar and non-thixotropic EPTT f -functionals have been investigated. Here, three key modifications have been implemented: first, that of convoluting EPTT and micellar Bautista–Manero f -functionals, either in a multiplicative ($Conv^*$) or additive ($Conv^+$) form; second, by adopting f -functionals in absolute form (ABS- f -correction); and third, by imposing pure uniaxial-extension velocity-gradient components at the pure-stretch flow-centreline (VGR-correction). With this combination of strategies, highly non-linear solutions have been obtained to impressively high Wi [$=O(5000+)$].

This capability permits analysis of industrial applications, typically displaying non-linear features such as thixotropy, yield stress and shear banding. The scope of applications covers enhanced oil-recovery, industrial processing of plastics and foods, as well as in biological and microfluidic flows. The impact of rheological properties across convoluting models (moderate-hardening, shear-thinning) has been observed through steady-state solutions and their excess pressure-drop (epd) production, stress, f -functional field structure, and vortex dynamics. Three phases of vortex-behaviour have been observed with rise in elasticity, along with upstream–downstream Moffatt vortices and plateauing epd -behaviour at high- Wi levels. Moreover, enhancement of positive-definiteness in stress has improved high- Wi solution attenuation.

© 2016 Elsevier B.V. All rights reserved.

1. Introduction

The theme of this study is particularly concerned with exploring predictive solutions for thixotropic worm-like micellar systems under medium to high elasticity conditions. To achieve this goal, convoluting hybrid constitutive models have been developed and embellished upon, utilising base Bautista–Manero (MBM) models to accommodate the dynamic micellar response, and grafting these upon exponential Phan–Thien–Tanner (EPTT) models for rubber-network response. The class of time-dependent MBM models follow those developed in [1–5]. In contrast, the time-independent network-based EPTT models were first proposed in [6], though more widely used today for many polymeric systems due to their inherently robust numerical characteristics. The work concentrates on the axisymmetric contraction–expansion flow problem, of geometric ratio 4:1:4 with rounded contraction-cap and recess-corners.

The issue of extraction of highly-elastic numerical prediction is tackled in a number of different directions. First, convolution of MBM and EPTT models is proposed, through their network-structure (f -) functionals, of multiplicative and additive forms. Second, and based on physical grounds, by appealing to only absolute values in structure-function dependency (ABS- f -correction), which controls non-linear response (see [5]). Third, through the problem approximation and its discretisation, via the imposition of consistent velocity gradient representation along the pure-stretch centreline of the flow (VGR-correction). The many relevant factors influencing the determination of particularly high elastic solutions (and their limitation in strain-hardening context) are discussed in depth in [5]. These aspects touch on: the numerical technique and discretisation for independent variables (stress, velocity, pressure, velocity-gradient); possible loss of IVP (Initial Value Problem) evolution and lack of positive definiteness retention (leading to stress-subsystem eigenvalue (s_i) analysis, s_i-N_I centreline relationship); the complex flow problem itself (sharp stress boundary layers, flow singularities); and the particular constitutive equation of choice [5].

* Corresponding author.

E-mail address: M.F.Webster@swansea.ac.uk (M.F. Webster).

Worm-like micelle solution systems are a versatile family of fluids, composed of mixtures of surfactants and salts. Typical surfactants are cetyltrimethylammonium bromide (CTAB) or cetylpyridinium chloride (CPyCl); common salts are sodium salicylate (NaSal) in water [4,7]. These components interact physically, depending on concentration, temperature and pressure conditions, to form elongated micelles. Such elongated constructs entangle and provoke mechanical interactions, stimulating breakdown and formation of internal structure [4]. This has consequences on the material properties of viscosity and elasticity. This complex constitution spurs highly complex rheological phenomena [7], and manifests features associated with thixotropy [1], pseudo plasticity [1–5], shear banding [8–13] and yield stress [14,15]. These systems have been coined ‘*smart materials*’, as their rheology dynamically adjusts to conform to prevailing environmental conditions. Such features render these systems as ideal candidates for varied processing and present-day applications. Examples of such application include use as drilling fluids in enhanced oil-reservoir recovery (EOR), additives in house-hold-products, paints, cosmetics, health-care products, and as drag reducing agents [4,7].

On *wormlike micellar modelling*, many approaches have been pursued to describe micellar flow behaviour. The original Bautista–Manero–Puig (BMP) model [1–2] consisted of the upper-convected Maxwell constitutive equation to describe the stress evolution, coupled to a kinetic equation to account for structural flow-induced changes and, was based on the rate of energy dissipation. Subsequently, Boek et al. [3] corrected the BMP model for its unbounded extensional viscosity in simple uniaxial extension – thus producing the base-form MBM model employed in the present analysis. This model has been implemented in complex flows such as in 4:1 contraction flow [16] and 4:1:4 contraction–expansion flow [4]. Therein, inconsistency has been exposed in excess pressure drop (*epd*) predictions at the Stokesian limit. Subsequently, this anomaly has been overcome [4] by including viscoelasticity within the structure construction–destruction mechanism. Two such model-variants have appeared, with energy dissipation given: (i) by the polymer contribution exclusively (NM- τ_p model, as adopted in the present article), and (ii) by the combination of the polymer and solvent contributions (NM-T model). These considerations have introduced new physics into the material response, by explicitly coupling thixotropic and elastic properties. Moreover, new key rheological characteristics have also been introduced, such as declining first normal stress difference in simple shear flow [4].

For completeness from the micellar literature, one may cite other alternative modelling approaches, though these have largely focused on simple flows and the shear-banding phenomena. The VCM (Vasquez–Cook–McKinley) model, based on a discrete version of the ‘*living polymer theory*’ of Cates, has been tested in simple flows, where rheological homogeneity prevails [17], and under conditions of shear-banding. VCM predictions captured the linear response of experimental shear data for CPyCl/NaSal concentrated solutions under small amplitude oscillatory shear and small amplitude step-strain experiments [18]. Moreover, Zhou et al. [19] found reasonable agreement with experimental data of Taylor–Couette and microchannel geometries and VCM predictions. Another approach consists of using the Johnson–Segalman model, modified with a diffusion term in the polymeric extra-stress equation (the so-called *d-JS* model) [20]. This model was found to predict shear-bands in cylindrical Couette flow. The Giesekus model has also been used in the representation of wormlike micelles under simple shear scenarios, whilst using the non-linear anisotropy coupling parameter to introduce shear-banding conditions [21]. Here under large amplitude oscillatory shear, a straightforward method was proposed to estimate the Giesekus non-linear parameter. Consequent Giesekus predictions were then found to lie

in quantitative agreement with data for low-concentration CTAB wormlike-micellar solutions.

Paper overview – in this article, convoluted equations of state are proposed based on the non-thixotropic network-based PTT and thixotropic micellar MBM parent models. Here, two convolution options have been devised, with additive (*Conv*⁺) and multiplicative (*Conv*^{*}) *f*-functionals. Their *rheometric response*, via shear and extensional data, has been correlated to that within axisymmetric 4:1:4 contraction–expansion complex flow solutions. In this respect, streamline patterns, N_1 -fields, *f*-functional and pressure-drops have been analysed. Moreover, *High-Wi solutions* [$Wi=O(5000+)$] are reported, achieved via ABS-*f*-correction and VGR-correction. Vortex activity has revealed a number of independent phases of interest. In this, upstream vortex enhancement has been identified at low elasticity levels, followed by complete suppression, somewhat reflecting strain-hardening/softening response. At high elasticity levels, a second stage of upstream–downstream vortex enhancement has been observed, along with secondary Moffatt vortices, of form suppressive-upstream and enhancing-downstream. The ABS-VGR correction (implying the simultaneous use of both ABS-*f* and VGR-corrections) delays any loss of positive definiteness, observed through reduced negativity of the *second eigenvalue* of the stress-subsystem, corresponding to the conformation tensor at the centreline. This has been correlated with *f*-functional values across the flow-field (now, $f \geq 1$), which grow as elasticity rises, thus ensuring positive viscosity estimation. *Excess pressure-drop (epd)* data asymptote to a plateau at high-*Wi* [$Wi=O(10^3)$]. At very high-*Wi* ($Wi > 10^3$), *epd*-data degenerate due to inconsistencies in inner-field to flow-outlet conditions. These inconsistencies are dealt with by imposing periodic boundary conditions at the inlet and outlet regions.

2. Governing equations, constitutive modelling and theoretical framework

2.1. Governing equations and constitutive models

The present flow context of interest is that of steady flow, under incompressible and isothermal conditions. In a non-dimensional framework, whilst assuming implied *notation on dimensionless variables (see on), the governing equations for mass conservation and momentum transport equations for viscoelastic flow become:

$$\nabla \cdot \mathbf{u} = 0, \quad (1)$$

$$\text{Re} \frac{\partial \mathbf{u}}{\partial t} = \nabla \cdot \mathbf{T} - \text{Re} \mathbf{u} \cdot \nabla \mathbf{u} - \nabla p. \quad (2)$$

Here, *t* represents time, an independent variable; the spatial gradient and divergence operators apply over the problem domain; field variables \mathbf{u} , *p* and \mathbf{T} represent fluid velocity, hydrodynamic pressure and stress contributions, respectively. Moreover, the total stress (\mathbf{T}) is split into two parts: identifying, a solvent component $\boldsymbol{\tau}_s$ (viscous-elastic $\boldsymbol{\tau}_s = 2\beta\mathbf{D}$) and a polymeric component $\boldsymbol{\tau}_p$. Then, $\mathbf{D} = (\nabla\mathbf{u} + \nabla\mathbf{u}^T)/2$ is the rate of deformation tensor, where the superscript ‘T’ denotes tensor transpose. Adopting appropriate scales below, corresponding dimensionless variables are defined as:

$$\mathbf{x}^* = \frac{\mathbf{x}}{L}, \quad \mathbf{u}^* = \frac{\mathbf{u}}{U}, \quad t^* = \frac{U}{L}t, \quad \mathbf{D}^* = \frac{L}{U}\mathbf{D},$$

$$\boldsymbol{\tau}_p^* = \frac{\boldsymbol{\tau}_p}{(\eta_{p0} + \eta_s)\frac{U}{L}}, \quad p^* = \frac{p}{(\eta_{p0} + \eta_s)\frac{U}{L}}.$$

A reference viscosity may be taken as the zero shear-rate viscosity ($\eta_{p0} + \eta_s$). Here, η_{p0} is the zero-rate polymeric-viscosity and η_s is the solvent-viscosity. Then, from this the solvent-fraction can

be defined as $\beta = \eta_s / (\eta_{p0} + \eta_s)$. The non-dimensional group number of Reynolds may be defined as $Re = \rho UL / (\eta_{p0} + \eta_s)$, where the material density is ρ . In the above, characteristic scales are U on fluid velocity (mean velocity, based on volume flow rate) and L on spatial dimension (based on minimum contraction-gap dimension). This provides a rate-scale of U/L , and the conventional common scaling on stress and pressure.

A second non-dimensional group number of Weissenberg ($Wi = \lambda_1 U/L$), governs elasticity, representing the product of a characteristic material relaxation time ($\lambda_1 = \frac{\eta_{p0}}{G_0}$), and a characteristic rate (U/L). Then, a general differential statement for the stress equation of state, provides the constitutive model as:

$$Wi \overset{\nabla}{\tau}_p = 2(1 - \beta)\mathbf{D} - f\tau_p. \quad (3)$$

Here, the notation implies use of the upper-convected derivative of extra-stress, $\overset{\nabla}{\tau}_p = \frac{\partial \tau_p}{\partial t} + \mathbf{u} \cdot \nabla \tau_p - \nabla \mathbf{u}^T \cdot \tau_p - \tau_p \cdot \nabla \mathbf{u}$. The networked nature of the fluid is then imbued through the f -functional.

With reference to the modelling of wormlike micellar systems, recently a new version of the MBM-model has been devised [4], with the *novel inclusion of viscoelasticity* within its thixotropic make-up – that is, responsive within the destruction mechanics of the fluid network structure. Commencing from the Bautista–Manero–Puig (BMP) model [1,2], and its Modified Bautista–Manero (MBM) model counterpart [3], a non-linear dimensional differential structure equation for the fluidity ($\phi_p = \eta_p^{-1}$) has emerged. It is from such fluidity that the polymeric viscosity function η_p may be extracted. Then, it is the distribution of the evolving space-time fluidity that generates the construction–destruction dynamics of the fluid network-structure. Typically, this may begin from a fully structured-state to be converted to one of a completely unstructured-state, using the energy dissipated by the material under flow.

The present paper appeals to a specific version of this class of models, that of $NM_{-\tau_p}$, which combines the viscoelasticity into the thixotropic dependency. This model variant drives structure destruction in the flow using the energy dissipated by the polymeric stress alone (see [4] for other options). Herein, dependency on fluidity ($\phi_p = \eta_p^{-1}$) arises through the dimensionless functional f , whose evolution is dictated by the generalised differential equation for structure:

$$\left(\frac{\partial}{\partial t} + \mathbf{u} \cdot \nabla \right) f = \frac{1}{\omega} (1 - f) + \xi_{G_0} Wi \tau_p : \mathbf{D}. \quad (4)$$

The dimensionless functional f is defined as $f = (\eta_{p0} / \eta_p)$, using η_{p0} as a viscous scaling factor on the fluidity. The dimensionless model parameters, which appear in the corresponding mechanistic terms, account for network-construction ($\omega = \lambda_s U/L$) and network-destruction [$\xi_{G_0} = (k/\eta_\infty) G_0 (\eta_{p0} + \eta_s)$].

At steady-state form, Eq. (4) collapses into its equivalent algebraic form,

$$f_{NM_{-\tau_p}} = 1 + \omega \xi_{G_0} Wi \tau_p : \mathbf{D}. \quad (5)$$

Note, in this form it is clear that the dissipation function is the driving influence in departure from Oldroyd behaviour ($f=1$); and that this is modulated by the product of the construction and destruction thixotropic-parameters with the Weissenberg number. Thus far, the dissipation function has adopted its natural sign – identified as the so called ‘natural-signed’ $NM_{-\tau_p}$ model.

The present study also calls upon the well-known exponential Phan–Thien/Tanner (EPTT) model, which finds its origin in rubber network-theory [6]:

$$f_{EPTT} = \exp\left(\frac{\varepsilon_{PTT}}{1 - \beta} Witr\tau_p\right). \quad (6)$$

The constant, non-dimensional PTT parameter $\varepsilon_{PTT} \geq 0$ largely dictates severity in strain-hardening, with smaller values limiting to zero, offering the greater extremes in extensional viscosity response (larger Trouton ratios). In the limit of vanishing $tr\tau_p$ or ε_{PTT} , f_{EPTT} tends to unity and classical Oldroyd-B behaviour is recovered. With such PTT models, $tr\tau_p$ is the function responsible for departure from Oldroyd-B form and represents the stored elastic energy of the material, see [22].

The EPTT model was selected given its bulk rheological shear-thinning and strain-softening properties, in common with micellar models (steady-state). The PTT model itself, was conceived to represent such bulk flow behaviour in rubber-network systems, based on a time-independent material-system construction [6]. Hence, in their combination with wormlike micellar networks, appropriate representation can be captured with time-dependent considerations built into the structural makeup. Under flow, these complex materials behave similarly to polymer solutions and melts; hence their naming ‘living polymers’ [23].

2.1.1. Convoluted models

In this work, and specifically with the aim of extracting high- Wi solutions in complex flow with rich rheological response, $NM_{-\tau_p}$ and EPTT steady-state f -functionals are combined to produce two new hybrid forms: (a) by product ($Conv^*$), and (b) by summation ($Conv^+$), viz.:

$$f_{Conv^*} = f_{EPTT} * f_{NM_{-\tau_p}}, \quad (7)$$

$$f_{Conv^+} = \frac{1}{2}(f_{EPTT} + f_{NM_{-\tau_p}}). \quad (8)$$

These combinations are conceived from the realisation that stronger f - Wi -functionalities render larger critical Wi numbers¹ (Wi_{crit}) in complex flow [5]. This has been confirmed earlier in [4], with $Conv^*$ for the same flow problem, where solutions for $Wi_{crit} = O(10^2)$ were attained without hints of numerical intractability. Models provided in [4], initiated our preliminary attempts (only multiplicative) in creating convoluted model-forms, but without the inclusion of the ABS- f and VGR corrections. Nevertheless, in [4] solutions were only report up to $Wi_{crit} = 300+$, whilst here the much wider range of high- Wi ($5000+$) is covered.

Moreover, the strategy of convolution employed is quite general in application, and can be extended equally over many other candidate classes of constitutive model. For example, one may contrast $NM_{-\tau_p}$ form [with a linear f - Wi relationship and $Wi_{crit} = 4.9$, see Eq. (5)], against that for EPTT [with an exponential f - Wi relationship and $Wi_{crit} = 210$, see Eq. (6)] [4]. The aim of the present paper is to capture such properties, calling upon hybrid models that inherit the functional strength of the EPTT model, alongside the thixotropic constructs of these wormlike-micellar models. This is strengthened by appealing to ABS- f and VGR-corrections described below, to extract solutions at ultra-high- Wi (demonstrated through micellar, LPTT and EPTT parent models [5]).

2.1.2. ABS- f -correction

Following [5], here a second approach adopted to increase Wi_{crit} -levels, is to embrace ABS-correction. This is based on providing positive f -functional values during flow evolution (time) and throughout the spatial domain in any single or mixed flow deformation. This is achieved by applying the absolute-value operation to those variable-components which trigger departure from Oldroyd-B response. Such correction was first proposed for micellar Bautista-Manero models [5]. Here across the domain during flow, the f -functional is a dimensionless fluidity that should remain

¹ Wi_{crit} is the largest Wi number for which stable numerical solutions are obtained.

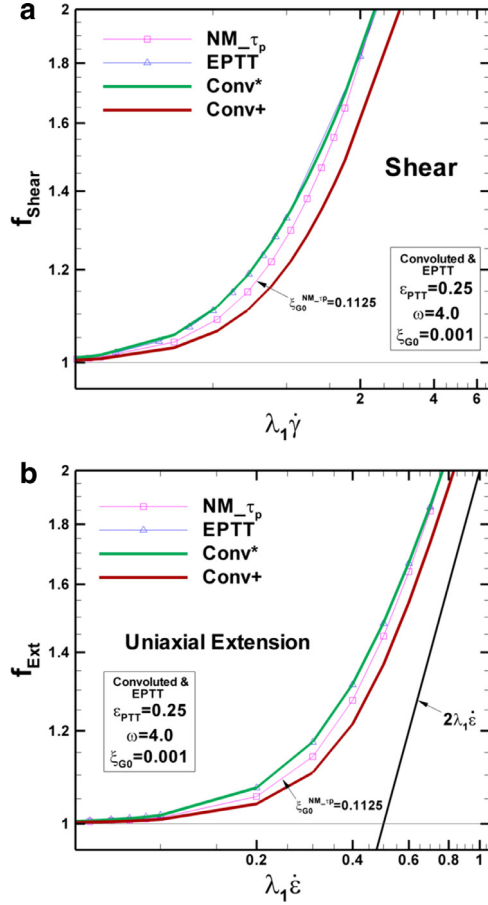


Fig. 1. f -functional in (a) simple shear and (b) uniaxial extensional flows, against Wi ; EPTT, NM_{τ_p} , $Conv^*$ and $Conv^+$; $\{\beta, \varepsilon_{PTT}, \omega, \xi_{C0}\} = \{1/9, 0.25, 4.0, 0.001\}$.

positive above unity, to avoid negative viscosity arising. Hence in steady-state form, the ABS- f -correction to NM_{τ_p} of Eqs. (4) and (5) yields ($NM_{\tau_p_ABS}$):

$$f_{NM_{\tau_p}}^{ABS} = 1 + \omega \xi_{C0} |Wi| \tau_p : \mathbf{D}. \quad (9)$$

In Eq. (9), the absolute-value sign is applied to every constituent component of the scalar dissipation-function (likewise for $tr\tau_p$ in EPTT). This concept may be generalised by implication to $Conv^*$ and $Conv^+$ f -functionals. In addition, the motivation for and consequences of the f -ABS functional-correction are enumerated as follows:

- In terms of thermodynamic arguments – it is intended to preserve positive dissipation acting on the material-structure f -functional and to drive non-linear response [5]. For these micellar fluids, the f -functional is explicitly related to the material viscosity. Hence, as demonstrated in [5], by avoiding negative dissipation-function values in the structure equation, one avoids the occurrence of non-physical negative viscosities.
- Moreover computationally, this f -functional correction aids in eliminating stress overshoot-undershoot, that frequently occur around regions of abrupt solution adjustment, such as near the contraction-tip and geometry-walls [4]. These sudden and localised solutions fluctuations have been correlated to ultimate intractability of steady-state solutions (and hence, attainment of high Wi_{crit}) [5].
- Finally, under ideal viscometric flow where only variable magnitudes apply, such f -functional correction is rendered redundant [5].

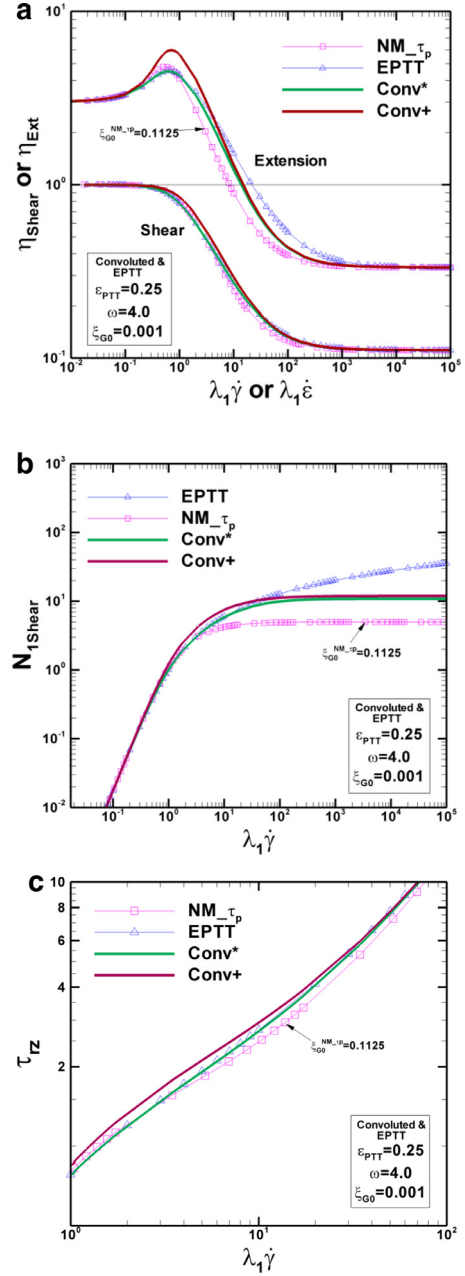


Fig. 2. (a) η_{Shear} , η_{Ext} , (b) N_{IShear} and (c) τ_{rz} against deformation rate; EPTT, NM_{τ_p} , $Conv^*$ and $Conv^+$; $\{\beta, \varepsilon_{PTT}, \omega, \xi_{C0}\} = \{1/9, 0.25, 4.0, 0.001\}$.

2.1.3. Material functions

In Figs. 1 and 2, material function response for the parent NM_{τ_p} and EPTT models considered are reported [4]. The solvent-fraction level and EPTT model ε_{PTT} -parameter considered in this work are $\{\beta, \varepsilon_{PTT}\} = \{1/9, 0.25\}$, as a standard benchmark. Against this, the resulting micellar extensional viscosity is matched. The micellar NM_{τ_p} construction and destruction parameters, matching EPTT extensional viscosity peak, are $\omega = 4.0$ and $\xi_{C0} = 0.1125$, respectively [4]. Accordingly, and specifically for the convoluted $Conv^*$ model, the destruction parameter requires adjustment for matching to $\xi_{C0} = 0.001$. Note, for $Conv^+$, $\xi_{C0} = 0.001$ is retained for comparison across convoluted models.

Ideal flow data may be classified by solving the f -functional equation under specific homogeneous deformation conditions. Under the generalised differential constitutive model of Eq. (3), the dimensional shear viscosity is $\eta_{Shear} = \eta_s + \frac{\eta_{p0}}{f}$ and the first

normal stress difference in shear-flow is $N_{1Shear} = \frac{2\lambda_1\eta_{p0}\dot{\gamma}^2}{f^2}$. As a consequence in simple shear-flow, the dimensional algebraic $Conv^*$ and $Conv^+$ f -equations become, respectively:

$$f_{Conv^*}^2 \ln \left[\frac{f_{Conv^*}}{1 + \lambda_s \frac{k}{\eta_\infty} G_0 \lambda_1 \frac{\eta_{p0}\dot{\gamma}}{f_{Conv^*}}} \right] - 2\varepsilon_{PTT} \lambda_1^2 \dot{\gamma}^2 = 0, \quad (10)$$

$$f_{Conv^+}^2 \ln \left[2f_{Conv^+} - \left(1 + \lambda_s \frac{k}{\eta_\infty} G_0 \lambda_1 \frac{\eta_{p0}\dot{\gamma}}{f_{Conv^+}} \right) \right] - 2\varepsilon_{PTT} \lambda_1^2 \dot{\gamma}^2 = 0. \quad (11)$$

As a counterpart and within simple uniaxial extension, the extensional viscosity is derived as $\eta_{Ext} = 3\eta_s + \frac{3\eta_{p0}f}{(f-2\lambda_1\dot{\epsilon})(f+\lambda_1\dot{\epsilon})}$, and the $Conv^*$ and $Conv^+$ f -equations become, respectively:

$$\ln \left[\frac{f_{Conv^*}}{1 + \frac{3\lambda_s \frac{k}{\eta_\infty} G_0 \lambda_1 \eta_{p0} \dot{\epsilon}^2 f_{Conv^*}}{(f_{Conv^*} - 2\lambda_1 \dot{\epsilon})(f_{Conv^*} + \lambda_1 \dot{\epsilon})}} \right] (f_{Conv^*} - 2\lambda_1 \dot{\epsilon})(f_{Conv^*} + \lambda_1 \dot{\epsilon}) - 6\varepsilon_{PTT} \lambda_1^2 \dot{\epsilon}^2 = 0, \quad (12)$$

$$\ln \left\{ 2f_{Conv^+} - \left[1 + \frac{3\lambda_s \frac{k}{\eta_\infty} G_0 \lambda_1 \eta_{p0} \dot{\epsilon}^2 f_{Conv^+}}{(f_{Conv^+} - 2\lambda_1 \dot{\epsilon})(f_{Conv^+} + \lambda_1 \dot{\epsilon})} \right] \right\} \times (f_{Conv^+} - 2\lambda_1 \dot{\epsilon})(f_{Conv^+} + \lambda_1 \dot{\epsilon}) - 6\varepsilon_{PTT} \lambda_1^2 \dot{\epsilon}^2 = 0. \quad (13)$$

In the above, the parent EPTT algebraic equation may be recovered, via either adopting $\lambda_s=0$ in the micellar construction term, or $k_\infty=(k/\eta_\infty)=0$ as the destruction parameter.

In Fig. 1, f -functional response is provided against deformation rate, for $Conv^*$ and $Conv^+$ model representations. This response is contrasted against parent NM_{τ_p} and EPTT data under simple shear flow (Fig. 1a) and simple uniaxial extensional flow (Fig. 1b).

One observes that f -functional slopes under uniaxial extension (Fig. 1b; in expanded-scale) are steeper than those under simple shear flow (Fig. 1a). Both forms display analogous rising trends with deformation-rate rise.

In simple shear flow (Fig. 1a) and the range $10^{-1} \leq \lambda_1 \dot{\gamma} \leq 1$, the initial slope of f - $Conv^+$ proves to be the shallowest, followed by NM_{τ_p} , and finally overlapping response of EPTT and $Conv^*$. Note, f - NM_{τ_p} response continually increases in slope and intersects EPTT and $Conv^*$ curves at $\lambda_1 \dot{\gamma} \sim 2.5$ (Fig. 1a). In contrast beyond $\lambda_1 \dot{\gamma} \geq 1.5$, EPTT, $Conv^+$ and $Conv^*$ data ultimately run parallel to one another. Consistently, and at any fixed deformation-rate, $Conv^+$ data display smaller f -values with respect to those of $Conv^*$, NM_{τ_p} and EPTT. These observations are analogous to simple uniaxial extension (Fig. 1b), but apply at earlier strain-rates.

In Fig. 2 shear and extensional data is provided, in the form of η_{Ext} , η_{Shear} , N_{1Shear} and τ_{rz} . In Fig. 2a, η_{Ext} -data provides the most significant departure across models, whilst differences in η_{Shear} response are less evident. Note, the drop at onset of shear-thinning for $Conv^+$ η_{Shear} starts at slightly larger shear-rates.

The $Conv^+$ η_{Ext} -peak is the largest and most prominent (at ~ 7 units), whilst EPTT, NM_{τ_p} and $Conv^*$ extrema attain about 6 units. These discrepancies in η_{Ext} -extrema correlate with the levels of f -functional response. Note in particular, $Conv^+$ response with the largest η_{Ext} -peak, provides the smallest f -functional response across the strain-rate range, and lies closest to the $f=2\lambda_1\dot{\epsilon}$ reference-line in Fig. 1b. Recall, this reference-line illustrates the f -pole, at which unbounded extensional viscosity results.

In the range $1 \leq \lambda_1 \dot{\epsilon} \leq 10$, $Conv^+$ η_{Ext} displays the largest overshoot and steepest decline in strain-softening (common to all models), intersecting with EPTT at $\lambda_1 \dot{\epsilon} \sim 4$ units, whilst $Conv^+$ η_{Ext} and $Conv^*$ η_{Ext} practically unite thereafter. For $4 \leq \lambda_1 \dot{\epsilon} \leq 10^3$, EPTT response dominates.

Table 1
{Critical, first-failure} Weissenberg numbers $\{Wi_{crit}, Wi_{fail}\}$ across models.

| Model | f | $Wi_{crit}, (Wi_{fail})$ | | |
|---------------|--|--------------------------|--------------|--------------|
| | | Natural Sign | ABS | ABS_VGR |
| NM_{τ_p} | $1 + \omega \xi_{c0} Wi \tau_p : D$ | 4.9, (5) | 39, (40) | 370, (380) |
| EPTT | $\exp(\frac{\xi_{c0}}{1-\beta} tr \tau_p)$ | 210, (220) | 4000, (4250) | 4250, (4500) |
| $Conv^*$ | $f_{EPTT} * f_{NM_{\tau_p}}$ | 224, (225) | 2500, (2750) | -, (5000+) |
| $Conv^+$ | $\frac{1}{2}(f_{EPTT} + f_{NM_{\tau_p}})$ | 67, (68) | 3000, (3250) | -, (5000+) |

The first-normal stress-difference in shear (N_{1Shear}) is provided in Fig. 2b. Here and at high shear-rates, both convoluted models inherit the limiting NM_{τ_p} plateau behaviour, but at relatively larger N_{1Shear} -levels than for raw NM_{τ_p} . In contrast, EPTT- N_{1Shear} monotonically rises with shear-rate. Throughout the range $1 \leq \lambda_1 \dot{\gamma} \leq 50+$, $Conv^+$ dominates in N_{1Shear} response (see above in η_{Ext}); so that at $\lambda_1 \dot{\gamma} \sim 50+$, EPTT and $Conv^+$ data-curves intersect, and EPTT domination succeeds.

By way of contrast, shear stress data (τ_{rz}) are recorded in Fig. 2c, using a zoomed-view for enhanced feature exposure. Throughout the range $1 \leq \lambda_1 \dot{\gamma} \leq 100$, τ_{rz} - $Conv^+$ dominate; NM_{τ_p} provides the minimum response for $\lambda_1 \dot{\gamma} \geq 3$ (intersecting with EPTT- $Conv^*$ below this level); EPTT and $Conv^*$ response overlap and are trapped between these two extremes. Note at very high shear-rates, the trend is to asymptote to a common τ_{rz} -behaviour.

2.2. Centreline VGR-correction, boundary conditions, critical Weissenberg number (Wi_{crit}) and fe–fv scheme

The concept behind VGR-correction on the centreline [5] is to eliminate noise proliferation, which may provoke numerically polluted solutions and thereby premature solution breakdown. In contraction–expansion flow on the symmetry centreline, uniaxial (inhomogeneous) pure-extension applies; on the contraction-wall (inhomogeneous) pure-shear flow prevails. Conventionally, along the contraction-wall, the so-called stick-boundary (rest) condition is assumed. Entry and exit flow conditions are then periodic in dynamics ($\nabla \mathbf{u}$), stress (τ_p) and velocity (\mathbf{u}) – noting the shear-thinning profile form and using feedback and feedforward in inlet and outlet regions for $\nabla \mathbf{u}$ and τ_p at high limits of $Wi \geq 500+$ (to preserve fully-developed flow). There is only necessity to set pressure at flow-exit, to impose a pressure level and remove pressure indeterminacy.

The VGR-correction is imposed only on the centreline, where specific analytical restrictions on the deformation gradients emerge. This enforces: (i) shear-free flow, to ensure 1D-extensional deformation (Eq. (14a)); (ii) a pure uniaxial extension relationship between the normal deformation-gradients (Eq. (14b)); and (iii) nodal-pointwise continuity imposed exactly, in discrete form (Eq. (14c)).

Assuming $\hat{\epsilon} = \frac{\partial u_z}{\partial z}$,² for extension-rate on the centreline in the axial direction, then the following identities may be established and imposed via VGR-correction:

$$\frac{\partial u_z}{\partial r} = \frac{\partial u_r}{\partial z} = 0, \quad (14a)$$

$$\frac{\partial u_r}{\partial r} = -\frac{1}{2} \frac{\partial u_z}{\partial z} = -\frac{1}{2} \hat{\epsilon}, \quad (14b)$$

$$\frac{u_r}{r} = -\left(\frac{\partial u_z}{\partial z} + \frac{\partial u_r}{\partial r} \right) = -\frac{1}{2} \hat{\epsilon}. \quad (14c)$$

Table 1 records the various levels of critical Weissenberg number attained in the simulations presented. Under the natural-signed

² As a function of z -spatial variable, in uniaxial extension along the flow centreline.

Table 2a
Mesh characteristics and Wi_{crit} .

| Level of refinement | Elements | Nodes | D.O.F. ^a (u, p, τ) | R_{min} | Wi_{crit}^b | Densities ^c |
|---------------------|----------|--------|---|-----------|---------------|------------------------|
| Coarse | 1080 | 2289 | 14,339 | 0.0099 | 5000+ | 20 |
| Medium | 1672 | 3519 | 22,038 | 0.0074 | 5000+ | 33 |
| Refined_A | 2112 | 4439 | 27,798 | 0.0058 | 5000+ | 40 |
| Refined_B | 5760 | 11,935 | 74,698 | 0.0037 | 5000+ | 80 |

^a Degrees of freedom.

^b Mesh-refinement study conducted with $Conv^+$ model under the parameters settings of $\{\beta, \varepsilon_{PTT}, \omega, \xi_{G0}\} = \{1/9, 0.25, 4, 0.001\}$.

^c Number of elements around the constriction.

Table 2b
 N_I @ centreline, mesh-refinement study.

| Level of refinement | Wi | N_I @ centreline ^a | | | |
|---------------------|-------|---------------------------------|-------|-------|-----|
| | | 10 | 100 | 250 | 500 |
| Coarse | 0.713 | 0.189 | 0.085 | 0.019 | |
| Medium | 0.700 | 0.188 | 0.085 | 0.019 | |
| Refined_A | 0.699 | 0.187 | 0.084 | 0.018 | |
| | Wi | 5 | 10 | 25 | |
| Coarse | 0.157 | 0.713 | 0.177 | | |
| Medium | 0.132 | 0.700 | 0.169 | | |
| Refined_A | 0.132 | 0.699 | 0.169 | | |
| Refined_B | 0.130 | 0.693 | 0.163 | | |

^a Sampling position around the constriction ($z \sim 0$).

configuration, $Conv^* Wi_{crit}^{Conv^*} = 224$ is larger than those for the primary model solutions, that is $NM_{\tau_p} Wi_{crit}^{NM_{\tau_p}} = 4.9$ and $Wi_{crit}^{EPTT} = 210$. In contrast, $Conv^+ Wi_{crit}^{Conv^+} = 67$ is significantly smaller compared to that of EPTT ($Wi_{crit}^{EPTT} = 210$), but still larger than that of NM_{τ_p} ($Wi_{crit}^{NM_{\tau_p}} = 4.9$). This diminished $Conv^+ Wi_{crit}$ correlates with the larger $Conv^+ \eta_{ext}$ peak relative to the $Conv^*$ response in ideal flows (see Fig. 2), and the smaller $Conv^+ f$ -functional response (Fig. 1).

Under ABS correction exclusively, Wi_{crit} is now significantly elevated, with respect to those for the natural-signed solutions. Indeed for $Conv^*$, the Wi_{crit} rise recorded is from 224 to 2500 (representing a single order-of-magnitude change), whilst $Conv^+$ solutions reflect two orders-of-magnitude change, from 67 to 3000.

Under combined and enhanced ABS_VGR correction, Wi_{crit} is still further advance to be located beyond $Wi = 5000$ for both $Conv^*$ and $Conv^+$ solutions.

In addition, a rigorous *mesh-refinement* study has been performed. This examination has been performed under the more stringent $Conv^+$ -model, enforcing ABS- f and VGR corrections simultaneously, under the parameters settings of $\{\beta, \varepsilon_{PTT}, \omega, \xi_{G0}\} = \{1/9, 0.25, 4, 0.001\}$. Mesh characteristics and their corresponding critical Weissenberg number Wi_{crit} are listed in Table 2a. Interestingly, Wi_{crit} for the four meshes considered is located beyond $Wi = 5000$. This may be understood in complex flow through Wi -rise, as a consequence of the practical attainment of so-called second Newtonian viscosity plateaux, in the rate-decade $10^2 < Wi < 10^3$. Correspondingly in viscometric flow and for these convoluted models at high deformation-rates, plateaux are displayed in η_{Shear} , η_{Ext} and $N_{I_{Shear}}$ response for $10^2 < Wi < 10^3$ (see Figs. 1 and 2). In addition, Fig. 3a displays N_I -profiles at the pure-extensional flow-centreline, covering data across three mesh-refinement levels for the relatively high-elasticity levels of $Wi = \{10, 100, 250, 500\}$. Hence, at each Wi -level in a sampling position about the constriction ($z \sim 0$), the variance in N_I more refined-mesh solutions across meshes (see Table 2b), shows a percentage deviation of the order of $\sim 0.1\%$. Moreover with Wi -rise, these pure-extension centreline N_I -profiles follow patterns of rising peak-intensification in the range $0.1 \leq Wi \leq 1$ (not

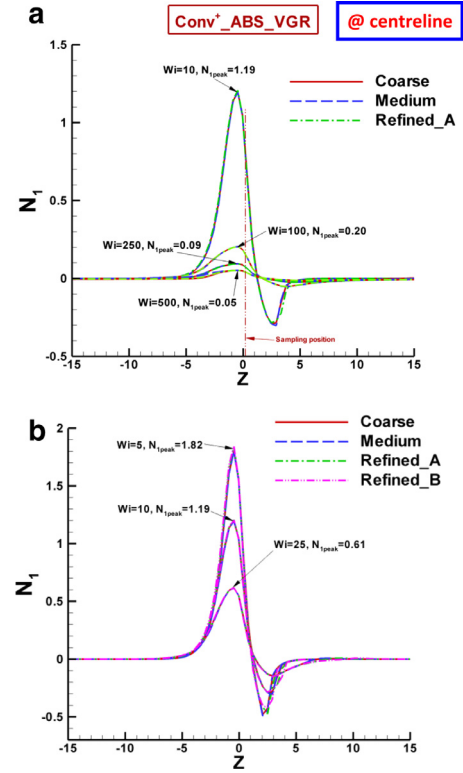


Fig. 3. Centreline- N_I against Wi ; mesh-refinement; (a) moderate-to-high $Wi = \{10, 100, 250, 500\}$, (b) low-to-high $Wi = \{5, 10, 25\}$; $Conv^+ \{\beta, \varepsilon_{PTT}, \omega, \xi_{G0}\} = \{1/9, 0.25, 4.0, 0.001\}$.

shown), and decline for $Wi > 1$. Such solution data may be correlated with the strain-hardening/softening features provided in simple uniaxial extension (Fig. 2a), and the gradual attainment of second Newtonian plateaux is exposed through vanishing centreline- N_I profiles with Wi -rise. In Fig. 3b, further evidence for solution mesh-convergence is provided, through centreline N_I -solution data over four successively-refined meshes and elasticity levels of $Wi = \{5, 10, 25\}$. This information draws upon solution data for an additional finer mesh (Refined_B; see Table 2b), with half the minimum mesh-spacing provided by the so-called Refined_A mesh. Here, over the more critical rising solution states, satisfactory solution mesh-convergence is gathered with mesh-refinement, as required. Beyond such Wi -levels as illustrated in Fig. 3a, the prevailing rheology provides only declining and merging solution trends, hence less stringent to pursue under the stronger refinement imposition of Refined_B mesh. One notes in passing and concerning algorithm convergence-rate, that previously a spatial convergence-rate of second-order has been reported for this implementation [24,25,29].

Hybrid finite element/finite volume scheme: The discrete approximation method is that of a hybrid finite element/volume scheme, as used elsewhere [26–29]. Such a scheme is a semi-implicit, time-splitting, fractional three-staged formulation, which invokes finite element (fe) discretisation for velocity-pressure (Q2–Q1) approximation and cell-vertex finite volume (fv) discretisation for stress, hence, combining the individual advantages and benefits offered by each approach.

Galerkin fe -discretisation is enforced on the embedded Navier–Stokes system components; the momentum equation at stage-1, the pressure-correction equation at stage-2 and the incompressibility satisfaction constraint at stage-3 (to ensure higher order precision). On solvers this leads to, a space-efficient element-by-element Jacobi iteration for stage-1 and -3; whilst for the

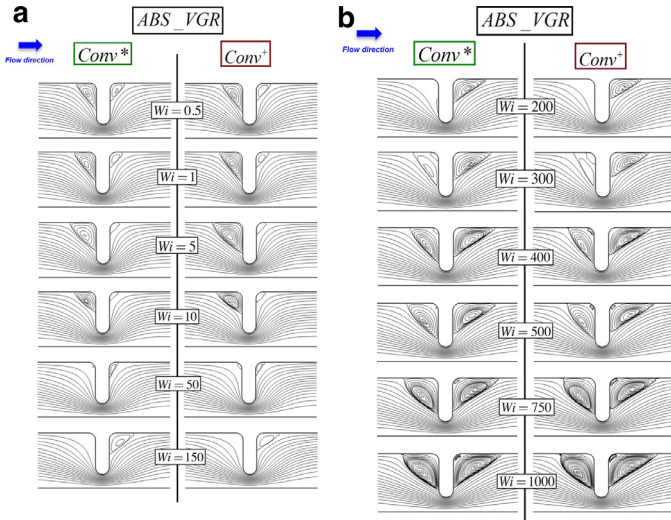


Fig. 4. (a) Streamlines against $Wi = [0.5, 150]$; ABS_VGR: $Conv^*$ and $Conv^+$; $\{\beta, \varepsilon_{PTT}, \omega, \xi_{C0}\} = [1/9, 0.25, 4.0, 0.001]$. (b) Streamlines against $Wi = [200, 1000]$; ABS_VGR: $Conv^*$ and $Conv^+$; $\{\beta, \varepsilon_{PTT}, \omega, \xi_{C0}\} = [1/9, 0.25, 4.0, 0.001]$.

pressure-correction stage-2, a direct Choleski solution method is utilised. In addition, a sub-cell cell-vertex fv -scheme is implemented for extra-stress, constructed on fluctuation-distribution for fluxes (upwinding) and median-dual-cell treatment for source terms.

Quadratic velocity interpolation is imposed on the parent fe triangular-cell, alongside linear interpolation for pressure. In contrast, the sub-cell fv -triangular-tessellation is constructed within the parent fe -grid by connecting the mid-side nodes. In such a structured tessellation, stress variables are located at the vertices of fv -sub-cells (cell-vertex method, equivalent to linear interpolation).

3. Vortex activity and streamline data: ABS_VGR inclusion, $Conv^*$ and $Conv^+$

The streamline patterns in Fig. 4, highlight in particular, the upstream and downstream vortex activity gathered, with respect to Wi -elevation, whilst covering the low to high range $0.5 \leq Wi \leq 1000+$. This affords rheological comparison in response across the two model variants of $Conv^*$ and $Conv^+$, under the combined ABS_VGR construct. Counterpart data is also included in Table 3 and vortex intensity trend plots of Fig. 5, where the limitations of ABS_VGR removal are indicated under Natural-model versions. This reveals the consequent premature Wi_{crit} -levels reached, and the appearance of Moffatt vortices (see Table 3 – quantities in brackets). Here, at $Wi=5$ (Fig. 4a), one notes larger and more active upstream vortex response with $Conv^+$ over $Conv^*$, a feature which may be correlated with the larger $Conv^+$ η_{ext} -peak, apparent in Fig. 2a. More generally, there is a first phase, of upstream vortex growth and downstream vortex suppression observed throughout the range $0.1 \leq Wi \leq 5$ (patterns in Fig. 4a; intensity in Fig. 5). $Conv^*$ Ψ_{min} -data peaks at $Wi=2$ ($-\Psi_{min}=4.68$); whilst $Conv^+$ Ψ_{min} -data peaks at $Wi=5$ ($-\Psi_{min}=8.20$).

Beyond this phase and for $5 < Wi \leq 50$ (Fig. 4a), upstream vortex suppression is apparent (softening/thinning effect), leading to practical vortex disappearance (by $Wi=50$ with $Conv^*$, by $Wi=75$ with $Conv^+$; sustained to $Wi=200$); in contrast, downstream vortex growth is just beginning (due to hardening, nb. also counterpart N_1 pattern below). In the range $0.1 \leq Wi \leq 50$, both $Conv^+$ and $Conv^*$ display downstream vortex suppression (Figs. 4a and 5). The only departure noted between downstream solution-data is over

Table 3

Vortex intensity ($\Psi_{min} = -\Psi_{min}^* \times 10^{-3}$) against Wi ; $Conv^*$, $Conv^+$ ($\{\varepsilon_{PTT}, \omega, \xi_{C0}\} = \{0.25, 4.0, 0.001\}$).

| Wi | | $\Psi_{min} = -\Psi_{min}^* \times 10^{-3}$ | | | |
|------|------------|---|----------------------------|-----------------|----------------------------|
| | | $Conv^*$ | | $Conv^+$ | |
| | | Natural | ABS_VGR | Natural | ABS_VGR |
| 0.1 | Upstream | 1.36 | 1.30 | 1.38 | 1.34 |
| | Downstream | 0.96 | 0.94 | 0.97 | 0.96 |
| 0.5 | Upstream | 2.17 | 1.79 | 2.24 | 2.24 |
| | Downstream | 0.40 | 0.46 | 0.39 | 0.39 |
| 1 | Upstream | 3.41 | 2.47 | 3.93 | 3.21 |
| | Downstream | 0.23 | 0.30 | 0.21 | 0.27 |
| 2 | Upstream | 6.23 | 4.68 | 9.38 | 7.39 |
| | Downstream | 0.11 | 0.16 | 0.10 | 0.14 |
| 5 | Upstream | 5.10 | 4.15 | 9.93 | 8.20 |
| | Downstream | 0.08 | 0.07 | 0.09 | 0.08 |
| 10 | Upstream | 0.91 | 0.94 | 1.90 | 1.92 |
| | Downstream | 0.10 | 0.04 | 0.23 | 0.08 |
| 15 | Upstream | 0.86 | 0.86 | 1.39 | 1.51 |
| | Downstream | 0.11 | 0.11 | 0.17 | 0.11 |
| 20 | Upstream | 0.34 | 0.32 | 0.49 | 0.47 |
| | Downstream | 0.11 | 0.03 | 0.15 | 0.06 |
| 50 | Upstream | 0.01 | ~0 | 0.01 | 0.01 |
| | Downstream | 0.09 | 0.04 | 0.07 | 0.05 |
| 75 | Upstream | ~0 | ~0 | ~0 ^a | ~0 |
| | Downstream | 0.14 | 0.17 | 0.08 | 0.17 |
| 100 | Upstream | ~0 | ~0 | ~0 | ~0 |
| | Downstream | 0.19 | 0.33 | 0.33 | 0.33 |
| 150 | Upstream | ~0 | ~0 | ~0 | ~0 |
| | Downstream | 0.58 | 0.88 | 0.46 | 0.46 |
| 200 | Upstream | 0.01 | ~0 | ~0 | ~0 |
| | Downstream | 1.27 | 1.64 | 1.13 | 1.13 |
| 250 | Upstream | 0.17 ^b | 0.13 | 0.05 | 0.05 |
| | Downstream | 1.70 | 2.41 | 2.01 | 2.01 |
| 300 | Upstream | 0.58 | (-7.65×10^{-3}) | 0.36 | (-1.93×10^{-2}) |
| | Downstream | 3.15 | | 2.91 | |
| 400 | Upstream | 1.90 | (-3.37×10^{-3}) | 1.74 | (-8.68×10^{-3}) |
| | Downstream | 4.47 | | 4.35 | |
| 500 | Upstream | 3.29 | (-3.29×10^{-4}) | 3.14 | (-5.66×10^{-3}) |
| | Downstream | 5.59 | | 5.24 | (-5.10×10^{-3}) |
| 750 | Upstream | 7.06 | | 7.84 | |
| | Downstream | 7.62 | (-6.71×10^{-3}) | 7.65 | (-2.65×10^{-2}) |
| 1000 | Upstream | 9.25 | | 10.10 | |
| | Downstream | 9.12 | (-1.49×10^{-2}) | 9.37 | (-3.92×10^{-2}) |
| 2000 | Upstream | 13.60 | | 14.48 | |
| | Downstream | 11.94 | (-3.61×10^{-2}) | 12.34 | (-7.11×10^{-2}) |
| 3000 | Upstream | 15.43 | | 14.66 | |
| | Downstream | 13.13 | (-4.89×10^{-2}) | 13.34 | (-9.93×10^{-2}) |
| 4000 | Upstream | 15.45 | | 15.66 | |
| | Downstream | 13.72 | (-6.50×10^{-2}) | 13.49 | (-1.1×10^{-2}) |
| 5000 | Upstream | 15.79 | | 16.34 | |
| | Downstream | 13.80 | (-7.07×10^{-2}) | 13.77 | (-1.1×10^{-2}) |

^a $Wi_{crit} = 67$.

^b $Wi_{crit} = 224$.

the restricted range $4 \leq Wi \leq 50$, where $Conv^+$ is less suppressive with Wi -rise than found for $Conv^*$ (Fig. 5). One notes however, under $Conv^*$, that suppression is so strong in this range, that the downstream vortex disappears by $Wi=50$.

These upstream vortex trends continue up to $Wi=200$, where for $Conv^+$ the upstream vortex has now been completely suppressed (Fig. 4b), whilst $Conv^*$ provides the first hints of appearance of a second contraction-frontface upstream vortex, located towards the contraction-cap. At this stage, both $Conv^+$ and $Conv^*$ provide considerably elongated downstream vortices.

At the further advanced stage of $50 \leq Wi \leq 1000+$ and beyond, downstream vortex growth persists, this proving relatively rapid and matching with both $Conv^+$ and $Conv^*$ (Figs. 4a, b and 5). Secondary Moffatt-vortices appear by $Wi=500$ ($Conv^+$) and $Wi=750$ ($Conv^*$), and strengthening subsequently (Fig. 4b; Table 3 – quantities in brackets). For both $Conv^+$ and $Conv^*$, this is accompanied with a secondary spurt of upstream vortex enhancement, after

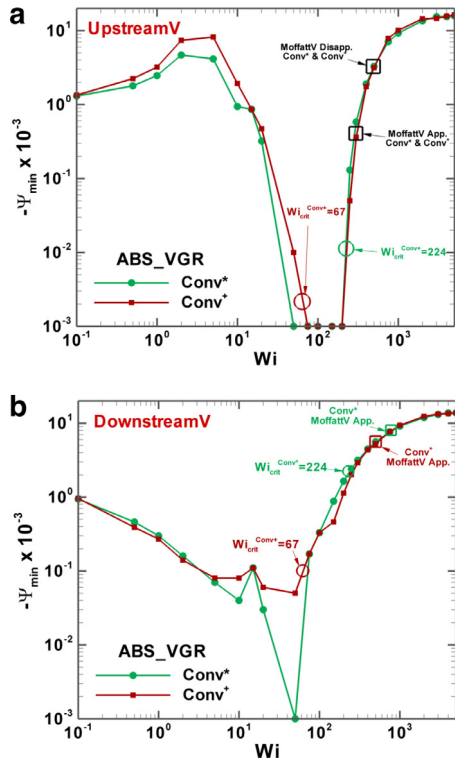


Fig. 5. (a) Upstream and (b) downstream vortex intensity against Wi ; $Conv^*$ and $Conv^+$, VGR_ABS; $\{\beta, \varepsilon_{PTT}, \omega, \xi_{CO}\} = \{1/9, 0.25, 4.0, 0.001\}$.

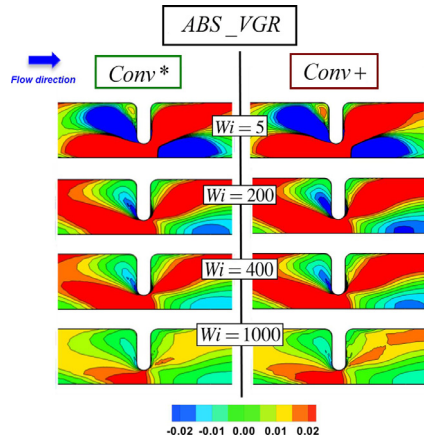


Fig. 6. N_1 against Wi ; ABS_VGR: $Conv^*$ and $Conv^+$; $\{\beta, \varepsilon_{PTT}, \omega, \xi_{CO}\} = \{1/9, 0.25, 4.0, 0.001\}$.

$Wi=200$ (Figs. 4b, and 5). In this upstream zone, the secondary Moffatt-vortex that appears by $Wi=300$, subsequently dies away by $Wi=500$, to be suppressed by $Wi=750+$. By $Wi=1000+$ and above, intense, enlarged and concave upstream and downstream streamline perimeters are observed (Fig. 4b). Hence, secondary-upstream Moffatt-vortices are ultimately suppressive, whilst those downstream are expansive (and stronger for $Conv^+$; Fig. 4b; Table 3 – quantities in brackets).

4. N_1 fields and vortex-like structures

Analysing Wi -increase under ABS_VGR: From the N_1 -fields in Fig. 6 and at $Wi=5$, $Conv^+$ displays a more intense vortex-like structure upstream of the contraction, corresponding to its relatively higher η_{ext} -peak (see Fig. 2a), and tying in with the streamline patterns above. For both convoluted solutions, a single

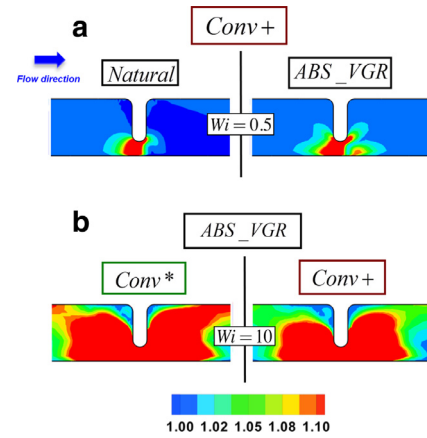


Fig. 7. f -functional against Wi ; (a) $Conv^+$: natural and ABS_VGR; (b) ABS_VGR: $Conv^*$ and $Conv^+$; $\{\beta, \varepsilon_{PTT}, \omega, \xi_{CO}\} = \{1/9, 0.25, 4.0, 0.001\}$.

red-positive zone is observed that crosses the contraction-plane, from upstream of the contraction with origin on the centreline, to downstream of the contraction with expansion outwards to reach the downstream contraction-wall. This mixed shear-extension, red-zone is pinched by two disjoint blue-negative zones; one upstream of the contraction, with base in the front-face of the contraction and bordering the upstream vortex-zone, and the other downstream of the contraction-plane with base on the centreline. This pattern is held to be representative of the prevailing contraction–expansion flow dynamics.

Next, switching attention to the relatively high elasticity level of $Wi=200$ above that at $Wi=5$, the N_1 -fields have shifted dramatically. Firstly, the red-positive region appears more squeezed about the contraction region, and now both of its tails (upstream and downstream) are connected to the contraction wall. By contrast, the blue-negative-valued N_1 -regions have shrunk (due to shear-thinning); upstream of the contraction-cap and downstream over the centreline. Its downstream zone has become separated from the positive-red region and been further convected downstream, reflecting a relatively smaller size and intensity than at $Wi=5$. Here, $Conv^+$ is consistently more intense still than with $Conv^*$, as justified by η_{ext} -peak of Fig. 2a in the downstream-centreline extension-zone, and by N_{1Shear} -peak of Fig. 2b in the upstream-cap shear-zone.

Upon reaching the still more advanced stage of $Wi=400$, such trends are continued through Wi -elevation, with the red-positive region now becoming even smaller; $Conv^*$ also shows disconnection from the upstream-wall. The downstream blue-negative region is further convected-downstream; it loses intensity and size, as does the contraction-cap zone (justified as above).

The largest extreme of elasticity considered is that of $Wi=1000+$, N_1 red-positive regions have shrunk dramatically, as have the blue-negative zones (due principally to shear-thinning, strain-softening effects). Downstream of the contraction-plane, the N_1 red-positive zone almost vanishes under $Conv^*$, and disconnects from the downstream-wall under $Conv^+$. The strong blue-negative zone at the centreline has almost disappeared downstream, by convection and through loss of intensity (strain-softening). This also applies to the strong blue-negative zone at the contraction-cap, but decline here is due to shear-thinning.

Natural vs ABS_VGR f -fields, $Conv^+$, $Wi=0.5$: Under such comparison of Fig. 7a, there are obvious shape changes to observe from rounded-red high f -values for Natural $Conv^+$, to that for $Conv^+$ (ABS_VGR). The key feature to highlight is the removal of the downstream negative-blue zone on the centreline with the Nat-

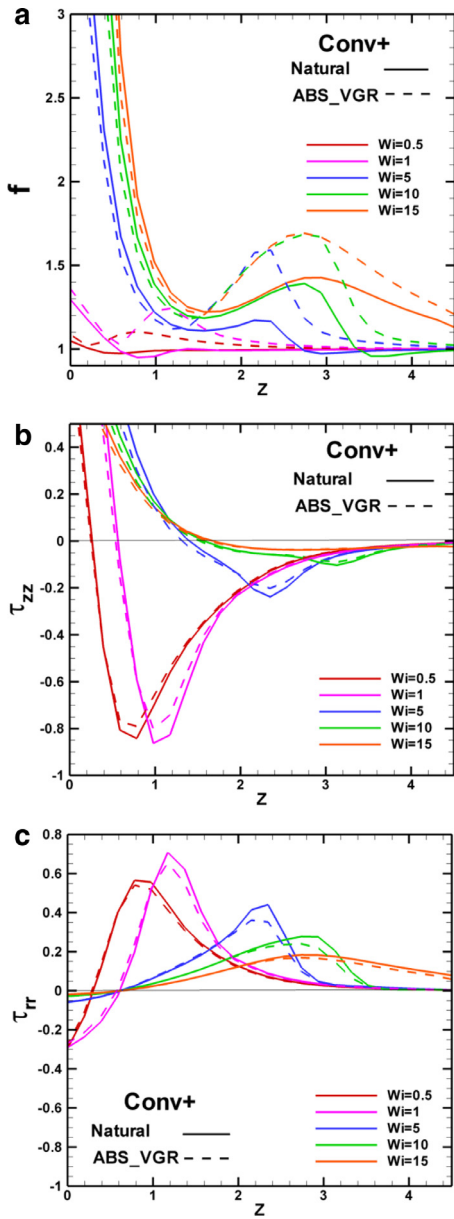


Fig. 8. (a) f -functional, (b) τ_{zz} , and (c) τ_{rr} , @ centreline against Wi ; $Conv^+$ natural and VGR_ABS; $\{\beta, \varepsilon_{PTT}, \omega, \xi_{C0}\} = \{1/9, 0.25, 4.0, 0.001\}$.

ural model version, and replacement with the positive-red zones of the $Conv^+$ (ABS_VGR) variant, along with larger f -extrema (as in Table 5).

This evidence is further supplemented by the $Conv^+$ -plots for rising Wi towards Wi_{crit} , with *Natural* vs *VGR_ABS* centreline-profiles of f -values and $\{\tau_{zz}, \tau_{rr}\}$ -values of Fig. 8; and in Fig. 9, with second stress-subsystem eigenvalue (s_2^{eig}), N_I -values and configuration-tensor components $\{\Pi_{zz}, \Pi_{rr}\}$. Kramers' rule identifies the relationship between stress and configuration tensor as: $\Pi = \tau_p + \frac{\eta_{p0}}{\lambda_1} I$. The choice here is for the $Conv^+$ -option, which is more dramatic in its data representation and with smaller Wi_{crit} -levels than the $Conv^*$ -option. Fig. 8 illustrates the fact that the ABS-version ensures $f \geq 1$ at all Wi -values, and hence retains positive viscosity levels (physically realistic), with corresponding N_I -values smaller in size (see Table 4) and smoother in profile-shape than for the *Natural*-signed version. Fig. 9 conveys the trends with rising Wi in possible loss-of-solution evolution through loss of positive-definiteness in the corresponding individ-

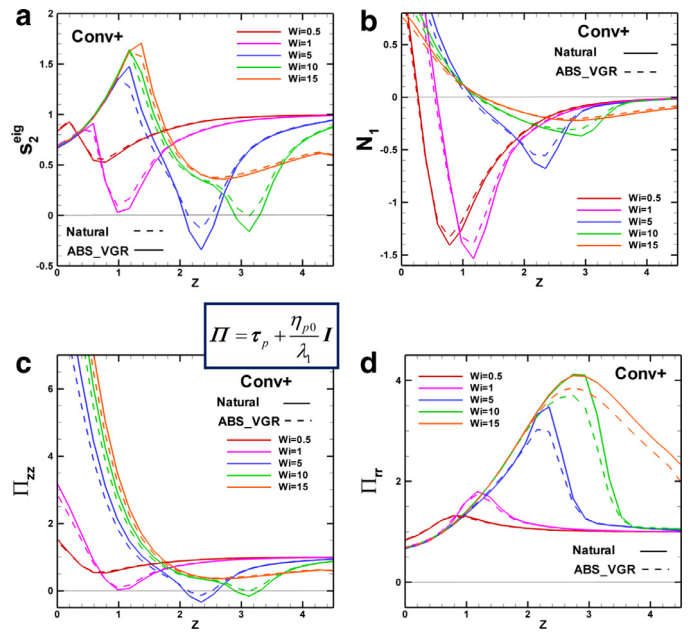


Fig. 9. (a) s_2 , (b) N_I , (c) Π_{zz} , (d) Π_{rr} @ centreline against Wi ; $Conv^+$ natural and VGR_ABS; $\{\beta, \varepsilon_{PTT}, \omega, \xi_{C0}\} = \{1/9, 0.25, 4.0, 0.001\}$.

Table 4

N_I maxima against Wi ; $Conv^*$, $Conv^+$ $\{\varepsilon_{PTT}, \omega, \xi_{C0}\} = \{0.25, 4.0, 0.001\}$.

| Wi | N_I | | | |
|------|-------------------|---------|-------------------|---------|
| | $Conv^*$ | | $Conv^+$ | |
| | Natural | ABS_VGR | Natural | ABS_VGR |
| 0.1 | 8.25 | 7.41 | 8.59 | 8.07 |
| 0.5 | 7.87 | 6.61 | 9.67 | 8.39 |
| 1 | 5.75 | 4.97 | 7.24 | 6.45 |
| 2 | 3.75 | 3.35 | 4.68 | 4.31 |
| 5 | 1.98 | 1.82 | 2.41 | 2.25 |
| 10 | 1.18 | 1.11 | 1.41 | 1.33 |
| 15 | 0.87 | 0.82 | 1.02 | 0.97 |
| 20 | 0.70 | 0.66 | 0.81 | 0.77 |
| 50 | 0.34 | 0.32 | 0.39 | 0.37 |
| 100 | 0.19 | 0.18 | 1.07 ^a | 0.21 |
| 200 | 0.11 | 0.10 | | 0.12 |
| 250 | 0.10 ^b | 0.09 | | 0.10 |
| 300 | | 0.07 | | 0.08 |
| 400 | | 0.06 | | 0.06 |
| 500 | | 0.05 | | 0.05 |
| 750 | | 0.03 | | 0.04 |
| 1000 | | 0.03 | | 0.03 |
| 2000 | | 0.01 | | 0.02 |
| 3000 | | 0.01 | | 0.01 |
| 4000 | | 0.01 | | 0.01 |
| 5000 | | 0.02 | | 0.02 |

^a $Wi_{crit}=67$.

^b $Wi_{crit}=224$.

ual configuration-tensor components. The superior VGR_ABS-option stability-wise performance over the *Natural*-option is apparent in the progressive states of second stress-subsystem eigenvalue (s_2^{eig}); just breaking the positivity requirement for the Wi -continuation-step of $Wi=5$ (note, not in true-time IVP-evolution, hence not catastrophic), but picking up subsequently. (s_2^{eig} -trends are more exaggerated in negativity for the *Natural*-option. Moreover, at each Wi -value, the configuration-tensor components (of Fig. 9c and d; centreline), relate directly to (s_2^{eig}), dependent upon the sign switch of N_I (as gathered from Fig. 9b), with $\{\Pi_{zz}\} = (s_2^{eig})$ if $N_I > 0$, and $\{\Pi_{rr}\} = (s_2^{eig})$ if $N_I < 0$ (see [5]).

Table 5
f-functional maxima against *Wi*; *Conv**, *Conv+* ($\{\varepsilon_{PTT}, \omega, \xi_{CO}\} = \{0.25, 4.0, 0.001\}$).

| <i>Wi</i> | <i>f</i> | | | |
|-----------|---------------------|-----------------------|---------------------|-----------------------|
| | <i>Conv*</i> | | <i>Conv+</i> | |
| | Natural | ABS_VGR | Natural | ABS_VGR |
| 0.1 | 1.15 | 1.24 | 1.08 | 1.13 |
| 0.5 | 2.49 | 2.60 | 2.09 | 2.14 |
| 1 | 4.10 | 4.23 | 3.54 | 3.60 |
| 2 | 6.80 | 7.02 | 6.14 | 6.18 |
| 5 | 13.43 | 13.58 | 12.30 | 12.52 |
| 10 | 23.14 | 23.51 | 21.23 | 21.48 |
| 15 | 32.47 | 32.88 | 29.86 | 29.95 |
| 20 | 41.48 | 41.98 | 38.58 | 38.35 |
| 50 | 98.25 | 94.90 | 96.97 | 87.96 |
| 100 | 196.08 | 179.86 | 130.25 ^a | 168.70 |
| 200 | 393.88 | 342.70 | | 323.64 |
| 250 | 433.75 ^b | 421.98 | | 404.22 |
| 300 | | 499.90 | | 485.72 |
| 400 | | 653.40 | | 648.39 |
| 500 | | 811.27 | | 809.95 |
| 750 | | 1216.22 | | 1214.11 |
| 1000 | | 1621.54 | | 1618.23 |
| 2000 | | 3254.83 | | 3248.77 |
| 3000 | | 5988.04 | | 10157.40 |
| 4000 | | 1.21×10^5 | | 25019.30 |
| 5000 | | 5.56×10^{10} | | 1.26×10^{14} |

^a $Wi_{crit} = 67$.
^b $Wi_{crit} = 224$.

Comparison across models, *Conv+* and *Conv**, *Wi* = 10: The comparison in Fig. 7b, displays a high-red *f*-zone under *Conv** that connects to the contraction-wall, both upstream and downstream. This is also relatively larger in *f*-maxima than under *Conv+* (see Table 5 for *f*-maxima comparison). In contrast, *Conv+* solution displays a red *f*-zone distribution pattern that is strictly confined about the contraction-plane with smaller values. This finding lies consistently in agreement with the relatively larger *Conv** *f*-values in simple-shear and simple uniaxial-extension (see Fig. 1). Moreover in N_1 -maxima (N_{1max} ; see Table 4), *Conv+* data rise in the range $0.1 \leq Wi \leq 0.5$, and then decline for $Wi > 0.5$; whilst *Conv** N_{1max} simply decline from $Wi \geq 0.1$. Here, *Conv+* somewhat reflects its relatively more exaggerated extensional viscosity features (Fig. 2a). Compared against *Conv** in the range $0.1 \leq \lambda_1 \dot{\varepsilon} \leq 1$, *Conv+* provides a more prominent strain-hardening response; then followed in $\lambda_1 \dot{\varepsilon}$ -rise by a steeper decline in strain-softening.

5. Excess pressure drop (epd)

5.1. Low-to-moderate *Wi*-levels, $0 \leq Wi \leq 50$

At low elasticity levels ($Wi < 1$; Fig. 10a), all *epd* data-curves for the five models follow the same declining trend, much attributed to the strong shear-thinning influence at this level of solvent-fraction of $\beta = 1/9$ and the level of N_1 over the range of rates considered (interpreted from larger solvent-fraction data elsewhere, see [4]).

As rates increase and for $Wi > 1$, *Conv+* data lies consistently above that for all other models, with most shallow slope of decline, prior to asymptoting to the high-rate plateau (which itself is dictated by the β -level). From these larger *epd-Conv+* values, one can argue that this effect is due to η_{ext} -over-estimation in this moderate rate range, whilst correspondingly η_{shear} has less variation across models (see Fig. 2). Moreover, N_1 is strengthened not weakened for *Conv+*-response; hence, would contribute a more suppressive effect on *epd* (see [30], for earlier justification argument). One also notes, the matching of *epd-EPTT* with *epd-Conv** on account

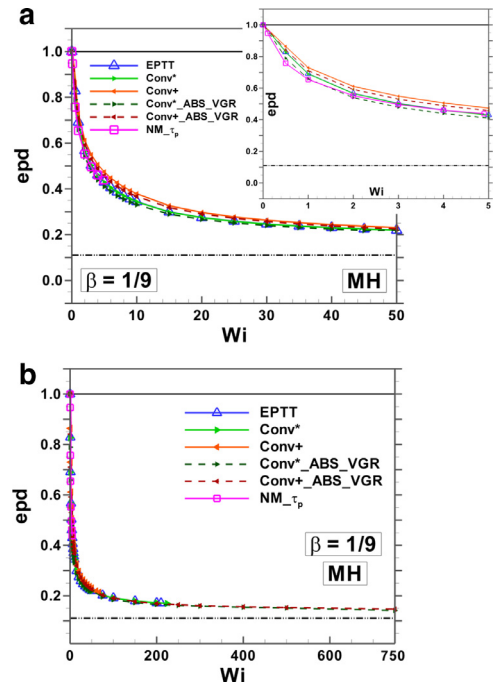


Fig. 10. *epd* against *Wi*; (a) low-to-moderate *Wi*, (b) high *Wi*; all models; $\{\beta, \varepsilon_{PTT}, \omega, \xi_{CO}\} = \{1/9, 0.25, 4.0, 0.001\}$.

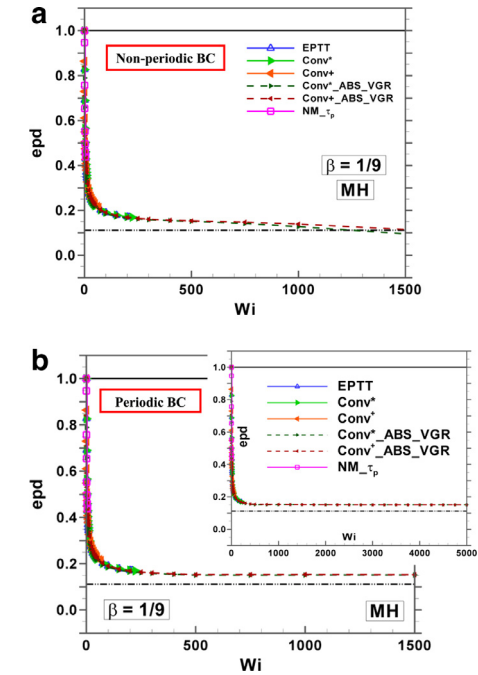


Fig. 11. *epd* against *Wi*; very high-*Wi* $Wi > 10^3$; all models; $\{\beta, \varepsilon_{PTT}, \omega, \xi_{CO}\} = \{1/9, 0.25, 4.0, 0.001\}$.

of matching rheology in $\{\eta_{ext}, \eta_{shear}, N_1\}$ within the moderate rate range.

5.2. High *Wi*-levels, $50 \leq Wi \leq 750$

In this exposition at high-deformation rates up to $Wi \sim 750$ (Fig. 10b), there is clear evidence for the ultimate take up of the *epd* plateau at $epd \sim 0.15$. This is borne out by the plateaux in material functions of Fig. 2; bar in EPTT- N_1 , which displays a limiting solution level of $Wi_{crit} = 220$. At even more extreme and very high

Wi -levels beyond 1000+ (Fig. 11), one notes that fully-developed exit conditions become increasingly more difficult to satisfy, with a requirement of ever longer exit zones. Shorter exit zones than necessary may impact upon the epd -measures, degrading them below the plateau level (Fig. 11a, non-periodic bc). Imposition of periodic boundary conditions (bc) on $\{\mathbf{u}, \nabla \mathbf{u}, \boldsymbol{\tau}_p\}$, with entry-exit zone feedback-feedforward on $\nabla \mathbf{u}$ and $\boldsymbol{\tau}_p$ as stated above, has been found to overcome this practical issue (Fig. 11b; see inset for solutions up to $Wi=5000+$ with periodic bc).

6. Conclusions

Here, additive ($Conv^+$) and multiplicative ($Conv^*$) convoluted models have been proposed, based on the thixotropic micellar MBM model and the non-thixotropic network-based EPTT model. Solutions at extremely high- Wi ($Wi=5000+$) and solvent-fraction $\beta=1/9$ have been attained – through the combination of ABS- f and VGR-corrections. In addition, consistency with mesh-refinement has also been addressed in this stringent highly polymeric-context, whilst covering an extensive range of elasticity levels. The main achievements in this work are borne out through – (i) an exploration of convoluted-model variants, via new combinations of f -functionals with some more well-known constitutive models; (ii) the exposition of necessity for periodic boundary conditions, in the capture of accurate and consistent pressure-drops at ultra-high $Wi > 1000$; (iii) the extraction of epd -plateau predictions at high- $Wi > 1000$; and (iv) the prediction of new and rich vortex dynamics for these material systems. Such vortex dynamics reveals, both upstream and downstream, enhancement and suppression, and Moffatt vortices at high- Wi . This information correlates closely with ideal viscometric response for these models (i.e. through extensional viscosity and N_{1Shear}). On EPD-plateau capture, this feature is attributed to attainment of second Newtonian-plateaux, as reflected in viscometric flow at high deformation-rates, via N_{1Shear} , shear viscosity and extensional viscosity.

On vortex dynamics and within the widely extended Wi -range, three distinct phases are detected in vortex dynamics: (i) upstream vortex enhancement and downstream vortex suppression in the range $0.1 \leq Wi \leq 5$; (ii) upstream vortex suppression and downstream vortex enhancement for $5 < Wi \leq 200$; and (iii) upstream and downstream vortex enhancement $200 \leq Wi \leq 1000+$. In the first stage, larger and more active upstream vortices are observed under $Conv^+$ response, which correlates with its larger η_{ext} -peak. In the second stage, upstream vortex suppression is apparent due to softening-thinning effects. This leads to upstream vortex disappearance (sustained to $Wi=200$). In contrast, downstream vortex growth begins. In the last stage, rapid downstream vortex growth occurs and is accompanied by a second stage of upstream vortex enhancement, under both $Conv^+$ and $Conv^*$. Moreover, secondary downstream Moffatt-vortices appear by $Wi=500$ ($Conv^+$) and $Wi=750$ ($Conv^*$), which strengthen with further Wi -rise. As a counterpart and in the range $200 \leq Wi \leq 500$, upstream Moffatt-vortices are apparent that behave in a suppressive manner with Wi -rise.

N_1 -field-data correspond with the streamline patterns at relatively low elasticity levels ($Wi=5$). Here, an upstream vortex-like structure is recorded, more intense under $Conv^+$, corresponding to vortex presence and its relatively higher η_{ext} -peak. At $Wi=200$, N_1 -fields dramatically change. Across convoluted models, $Conv^+$ N_1 -field-data is still more intense than in $Conv^*$ solutions, consistent with stronger $Conv^+$ η_{ext} -peak (associated with extension-dominated centreline trends) and with larger N_1 -peaks at medium-to-high shear-rates (associated wall shear-dominated zone). At extreme levels of $Wi=1000+$, N_1 values decline due principally to shear-thinning and strain-softening effects.

On f -functional and positive definiteness – the ABS model-version ensures $f \geq 1 \forall Wi$ -values, and hence retains positive viscosity, with corresponding smaller N_1 -values and smoother centreline profile-shape than for the Natural-signed version. Across models, larger $Conv^*$ f -maxima are recorded, which correlate with larger $Conv^*$ - Wi_{crit} . Moreover, the VGR_ABS-option performs in a superior manner (stability-wise) to the Natural-option, observed through the second eigenvalue (s_2^{eig}) of the stress-subsystem for the conformation-tensor. Here, VGR_ABS solutions only marginally conflict with the positivity-retention requirement (to avoid ensuing loss of IVP-evolution in time), whilst transcending the Wi -continuation-step at $Wi=5$, but subsequently recovering at larger Wi -levels. In contrast, Natural-signed s_2^{eig} -trends are more exaggerated in exposure to such negativity in (s_2^{eig}).

On excess pressure-drop and at low elasticity levels ($Wi < 1$), all epd data-curves decline, much attributed to strong shear-thinning (exaggerated at this solvent-fraction $\beta=1/9$ and N_{1Shear} levels). At larger $Wi > 1$, $Conv^+$ data dominates, with most shallow slope of decline. This may be correlated to η_{ext} -over-estimation in the moderate rate range, as η_{Shear} -data barely change across models. In the high- Wi range of $200 \leq Wi \leq 1000$, epd -asymptotes to the plateau-level of $epd \sim 0.15$, which may be associated with the plateaux observed in material functions at high deformation-rates. At very high- Wi levels [$Wi=O(5000+)$], fully-developed exit conditions become more difficult to satisfy. Here, application of periodic boundary conditions at the inlet and outlet flow regions become more appropriate.

Acknowledgements

Financial support (scholarship to J.E.L.-A.) from Consejo Nacional de Ciencia y Tecnología (CONACYT, México), Zienkiewicz College of Engineering scholarship and NHS-Wales Abertawe Bro Morgannwg Trust-fund, is gratefully acknowledged.

References

- [1] F. Bautista, J.M. de Santos, J.E. Puig, O. Manero, Understanding thixotropic and antithixotropic behavior of viscoelastic micellar solutions and liquid crystalline dispersions. I. The model, *J. Non-Newton. Fluid Mech.* 80 (1999) 93–113.
- [2] O. Manero, F. Bautista, J.F.A. Soltero, J.E. Puig, Dynamics of worm-like micelles: the Cox–Merz rule, *J. Non-Newton. Fluid Mech.* 106 (2002) 1–15.
- [3] E.S. Boek, J.T. Padding, V.J. Anderson, P.M.J. Tardy, J.P. Crawshaw, J.R.A. Pearson, Constitutive equations for extensional flow of wormlike micelles: stability analysis of the Bautista–Manero model, *J. Non-Newton. Fluid Mech.* 126 (2005) 29–46.
- [4] J.E. López-Aguilar, M.F. Webster, H.R. Tamaddon-Jahromi, O. Manero, A new constitutive model for worm-like micellar systems – numerical simulation of confined contraction–expansion flows, *J. Non-Newton. Fluid Mech.* 204 (2014) 7–21.
- [5] J.E. López-Aguilar, M.F. Webster, H.R. Tamaddon-Jahromi, O. Manero, High-Weissenberg predictions for micellar fluids in contraction–expansion flows, *J. Non-Newton. Fluid Mech.* 222 (2015) 190–208.
- [6] N. Phan-Thien, R.L. Tanner, A new constitutive equation derived from network theory, *J. Non-Newton. Fluid Mech.* 2 (1977) 353–365.
- [7] J. Yang, Viscoelastic wormlike micelles and their applications, *Curr. Opin. Colloid Interface Sci.* 7 (2002) 276–281.
- [8] F. Bautista, J.F.A. Soltero, J.H. Pérez-López, J.E. Puig, O. Manero, On the shear banding flow of elongated micellar solutions, *J. Non-Newton. Fluid Mech.* 94 (2000) 57–66.
- [9] P.D. Olmsted, Perspectives on shear banding in complex fluids, *Rheol. Acta* 47 (2008) 283–300.
- [10] S. Manneville, Recent experimental probe of shear banding, *Rheol. Acta* 47 (2008) 301–318.
- [11] J.F. Berret, R.G. Weiss, P. Terech, Rheology of wormlike micelles: equilibrium properties and shear-banding transitions, *Molecular Gels. Materials with Self-assembled Fibrillar Networks*, Springer, Amsterdam, 2006, pp. 667–720.
- [12] J.P. Rothstein, Strong flows of viscoelastic wormlike micelle solutions, in: D.M. Binding, K. Walters (Eds.), *Rheology Reviews*, The British Society of Rheology, Aberystwyth, Wales, UK, 2008.
- [13] M.A. Fardin, T. Divoux, M.A. Guedeau-Boudeville, I. Buchet-Maulien, J. Browaeys, G.H. McKinley, S. Manneville, S. Lerouge, Shear-banding in surfactant wormlike micelles: elastic instabilities and wall-slip, *Soft Matter* 8 (2012) 2535–2553.

- [14] F. Calderas, E.E. Herrera-Valencia, A. Sanchez-Solis, O. Manero, L. Medina-Torres, A. Renteria, G. Sanchez-Olivares, On the yield stress of complex materials, Korea-Aust. Rheol. J. 25 (2013) 233–242.
- [15] J.E. López-Aguilar, M.F. Webster, H.R. Tamaddon-Jahromi, O. Manero, Numerical modelling of thixotropic and viscoelastoplastic materials in complex flows, Rheol. Acta 54 (2015) 307–325.
- [16] H.R. Tamaddon-Jahromi, M.F. Webster, J.P. Aguayo, O. Manero, Numerical investigation of transient contraction flows for worm-like micellar systems using Bautista–Manero models, J. Non-Newton. Fluid Mech. 166 (2011) 102–117.
- [17] P.A. Vazquez, G.H. McKinley, L.P. Cook, A network scission model for wormlike micellar solutions: I. Model formulations and viscometric flow predictions, J. Non-Newton. Fluid Mech. 144 (2007) 122–139.
- [18] C.J. Pipe, N.J. Kim, P.A. Vazquez, L.P. Cook, G.H. McKinley, Wormlike micellar solutions: II. Comparison between experimental data and scission model predictions, J. Rheol. 54 (2010) 881–913.
- [19] L. Zhou, G.H. McKinley, L.P. Cook, Wormlike micellar solutions: III. VCM model predictions in steady and transient shearing flows, J. Non-Newton. Fluid Mech. 211 (2014) 70–83.
- [20] P.D. Olmsted, O. Radulescu, C.Y.F. Lu, Johnson–Segalman model with a diffusion term in a cylindrical Couette flow, J. Rheol. 44 (2000) 257–275.
- [21] A.K. Gurron, N.J. Wagner, Large amplitude oscillatory shear (LAOS) measurements to obtain constitutive equation model parameters: Giesekus model of banding and nonbanding wormlike micelles, J. Rheol. 56 (2012) 333–351.
- [22] M.A. Hulsen, A sufficient condition for a positive definite configuration tensor in differential models, J. Non-Newton. Fluid Mech. 38 (1990) 93–100.
- [23] R.G. Moss, J.P. Rothstein, Flow of wormlike micelle solutions past a confined circular cylinder, J. Non-Newton. Fluid Mech. 165 (2010) 1505–1515.
- [24] M.F. Webster, H.R. Tamaddon-Jahromi, M. Aboubacar, Transient viscoelastic flows in planar contractions, J. Non-Newton. Fluid Mech. 118 (2004) 83–101.
- [25] M.S. Chandio, M.F. Webster, D.M. Binding, N.E. Hudson, J. Mewis, J.-M. Piau, C.J.S. Petrie, P. Townsend, M.H. Wagner, K. Walters, On consistency of cell-vertex finite volume formulations for viscoelastic flow, in: Proceedings of the XIII International Congress on Rheology, Cambridge, vol. 2, British Society of Rheology, Glasgow, 2000, pp. 208–210.
- [26] H. Matallah, P. Townsend, M.F. Webster, Recovery and stress-splitting schemes for viscoelastic flows, J. Non-Newton. Fluid Mech. 75 (1998) 139–166.
- [27] F. Belblidia, H. Matallah, M.F. Webster, Alternative subcell discretisations for viscoelastic flow: velocity-gradient approximation, J. Non-Newton. Fluid Mech. 151 (2008) 69–88.
- [28] M.F. Webster, H.R. Tamaddon-Jahromi, M. Aboubacar, Time-dependent algorithms for viscoelastic flow: finite element/volume schemes, Numer. Methods Part. Differ. Equ. 21 (2005) 272–296.
- [29] P. Wapperom, M.F. Webster, A second-order hybrid finite-element/volume method for viscoelastic flows, J. Non-Newton. Fluid Mech. 79 (1998) 405–431.
- [30] H.R. Tamaddon-Jahromi, M.F. Webster, P.R. Williams, Excess pressure drop and drag calculations for strain-hardening fluids with mild shear-thinning: contraction and falling sphere problems, J. Non-Newton. Fluid Mech. 166 (2011) 939–950.